Advanced Energy Materials

ADVANCED ENERGY MATERIALS
www.advenergymat.de

RESEARCH ARTICLE OPEN ACCESS

Fluorinated Methylammonium Cation Containing Perovskite Solar Cells With Over 25% Power Conversion Efficiency

Justina Mikuciunaite[1] | Bin Ding[2] | Yuxuan Yang[3] | Xiao-Xin Gao[2] | Vida Valipour[4] | Yong Ding[2] | Negar Ashari Astani[4] | Jan Romano-deGea[2] | Lindsey E. K. Frederiksen[2] | Farzaneh Fadaei Tirani[2] | Vytautas Getautis[1] | Yi Zhang[3] | Mohammad Khaja Nazeeruddin[5,6] | Kasparas Rakstys[1]

[1]Department of Organic Chemistry, Kaunas University of Technology, Kaunas, Lithuania | [2]Institute of Chemical Sciences and Engineering, École Polytechnique Fédérale de Lausanne (EPFL), Lausanne, Switzerland | [3]Institute of Molecular Plus, School of Chemical Engineering and Technology, Tianjin University, Tianjin, People's Republic of China | [4]Department of Physics and Energy Engineering, Amirkabir University of Technology, Tehran, Iran | [5]Institute of Perovskite Photovoltaics and Integrated Optoelectronics (IPO), School of Integrated Circuits, Southeast University, Wuxi, Jiangsu, People's Republic of China | [6]Mechanical and Energy Engineering Department, College of Engineering, Imam Abdulrahman Bin Faisal University, Dammam, Saudi Arabi

Correspondence: Negar Ashari Astani (ashari@aut.ac.ir) | Yi Zhang (yi_zhang@tju.edu.cn) | Mohammad Khaja Nazeeruddin (mk.nazeeruddin@seu.edu.cn) | Kasparas Rakstys (kasparas.rakstys@ktu.lt)

Received: 2 January 2026 | **Revised:** 26 June 2026 | **Accepted:** 22 July 2026

Keywords: A-site | cation | fluorinated | methylammonium | perovskite | solar cell

ABSTRACT

High-performance perovskite solar cells (PSCs) are typically made using formamidinium $CH(NH_2)_2^+$ (FA^+), cesium $Cs^{+,}$ and the thermally unstable methylammonium $CH_3NH_3^+$ (MA^+) monovalent cations. Excluding unstable MA^+ leads to perovskite compositions with increased stabilities and decreased bandgaps. This study introduces a novel approach using a simple fluorinated methylammonium $CFH_2NH_3^+$ (FMA^+) cation capable of doping into the perovskite-framework. With the addition of an optimized quantity of 0.8 mol% FMAI, perovskite compositions are thermally more stable, enabling more reproducible n-i-p PSC performance with a power conversion efficiency of 25.67%. The PSCs exhibit operational stability over 2000 h. Spectroscopic and computational analyses suggest that FMAI may play a dual role as a fluorinated ammonium additive capable of doping into the perovskite and as a chemically non-innocent precursor producing passivating species.

1 | Introduction

Organic–inorganic lead halide perovskite materials have attracted considerable interest for optoelectronic applications, including solar cells [1–4], light-emitting diodes [5–7], lasers [8, 9], detectors [10, 11], and sensors [12, 13]. Perovskite solar cells (PSCs), which use organic–inorganic lead halides as the photoactive layer, have shown a rapid increase in power conversion efficiency (PCE) since their first demonstration, from 3.8% in 2009 to a certified value of 28% in 2026 [14]. Despite this progress, the long-term instability toward moisture, heat, and light of PSCs containing 3D perovskite layers remains a major challenge for commercialization [15, 16]. Therefore, strategies such as compositional tuning, defect passivation, and crystal-growth regulation through precursor-solution engineering have been widely explored to improve device stability without sacrificing efficiency [17–20].

Optimizing the composition of the perovskite photoactive layer is an important target for the further improvement of the performance of perovskite-based photovoltaics. The phase stability of the $APbX_3$ perovskite structure is governed, together with

thermodynamic factors, by the size and geometry of the A-site cation, which can be approximated by Goldschmidt's tolerance factor [21–24]. Currently, Cs^+ and FA^+ cations are widely used in high-efficiency PSCs due to their high stability and favorable red-shifted bandgap [21–24]. In contrast, MA^+ is generally regarded as a key risk factor for long-term operational stability because of its higher volatility and lower thermal stability [25, 26]. Pure $MAPbX_3$, $FAPbX_3$, or $CsPbX_3$ ($X = Br^-$ or I^-) perovskites can suffer from thermal or structural instability depending on the halide composition and processing conditions [27–32]. Mixed-cation and mixed-halide strategies are therefore commonly used to access desirable bandgaps, improve crystallization, and enhance structural stability [33]. However, increasingly complex mixed-cation/mixed-halide compositions may also be susceptible to photo-, thermal-, or bias-induced segregation during operation [34].

A-site cation compositional engineering offers opportunities to tune stability and optoelectronic properties. Undersized cations, such as K^+ or Rb^+, may be incorporated along the surfaces and grain boundaries, or other structurally accessible sites [35, 36], whereas oversized organic cations typically form lower-dimensional phases, such as 2D perovskites [37–40]. Oversized organic cations typically form lower-dimensional phases. Bulky fluorinated organic cations have also been used to improve long-term durability, due to their hydrophobic character and interfacial passivation effects [41–44]. The introduction of fluorine-containing additives in the A-sites can increase the molecular dipole moment, alter electrostatic interactions within the inorganic framework, and potentially improve the optical absorption capacity and structural and thermal stability. Hence, fluorinated methylammonium cations ($CH_{(3-n)}F_nNH_3^+$ or F_nMA^+, n = 1, 2, 3) are therefore attractive because they combine the small size required for compatibility with the 3D perovskite framework with the electronic effects of fluorination. Although such advantages of fluorinated methylammonium cations have been theoretically predicted and reported, the limited availability of such cations hinders experimental realization [45–48]. In principle, fluorinated methylammonium iodide salts could be synthesized by simply reacting fluorinated methylamines with hydroiodic acid. However, the very low stability of halogenated methylamines hinders the preparation of fluorinated methylammonium salts via this route.

In this work, we report the synthesis of fluoromethylammonium iodide (CH_2FNH_3I or FMAI) through a simple nucleophilic addition reaction between fluoroiodomethane and ammonia in methanol. We then evaluate FMAI as a low-concentration fluorinated additive for FA/Cs-based PSCs. An optimized FMAI loading of 0.8 mol% improves film quality, suppresses degradation, and enhances photoluminescence response, affording devices with a stabilized PCE exceeding 25.5% and improved operational stability over 2000 h. We investigated the mechanism of action of FMAI using complementary experimental and computational approaches, revealing the dual role of FMAI, in which the additive can act both as a fluorinated ammonium cation capable of doping into the perovskite-framework, leading to defect passivation and phase stabilization, and as a reactive additive that may form additional species during film formation and operation.

2 | Results and Discussion

Fluoromethylammonium iodide (FMAI) was obtained as a white solid in 41% yield via a simple nucleophilic addition reaction between fluoroiodomethane and ammonia in methanol. The compound was fully characterized by ^1H, ^{13}C, and ^{19}F NMR spectroscopy and mass spectrometry with characterization data provided in the Supporting Information) [49]. Attempts to prepare difluoromethylammonium iodide (CHF_2NH_3I) and trifluoromethylammonium iodide (CF_3NH_3I) using the same procedure, starting from difluoroiodomethane and trifluoroiodomethane, respectively, were unsuccessful.

To assess whether FMA^+ could potentially dope into a 3D lead-halide perovskite framework, we evaluated conventional stability descriptors for A-site cation incorporation, namely the Goldschmidt factor (t) and Li's octahedral factor (μ) [50]. Although the calculated tolerance factor for $FMAPbI_3$, $t = 1.01$, is slightly above the conventional 0.8–1.0 range, it is close enough to suggest that FMA^+ is not prohibitively oversized for a 3D lead-halide framework, motivating a more detailed computational investigation. Moreover, the calculated octahedral factor, $\mu = 0.541$, also satisfies the commonly used $\mu > 0.41$ criterion [50].

To examine how the incorporation of FMAI may impact the $FAPbI_3$ lattice, the formation energy ($E_{formation}$) and the relative phase stability of the FMAI-doped perovskite with varying percentages of FMAI were assessed using periodic Density Functional Theory (DFT) calculations of the crystalline system (full details of DFT calculations and the corresponding files are given in the Supporting Information) [51–53]. $E_{formation}$ was calculated using the following equation [54]:

$$E_{formation} = E_{(FMAI)_x(FAI)_{1-x}(PbI_2)} - xE_{FMAI} - (1-x)E_{FAI} - E_{PbI_2}$$

where $E_{(FMAI)_x(FAI)_{1-x}(PbI_2)}$, E_{FMAI}, E_{FAI}, and E_{PbI_2} are the total energies of the precursors PbI_2 (trigonal phase), FAI, and FMAI (both cubic phases) obtained from DFT calculations [55]. The results indicate a linear increase in $E_{formation}$ of the perovskite with increasing doping of FMA^+, which remains negative up to 58% of FMA^+ incorporation, when presumably the strain in the lattice leads to instability. We calculated the relative phase stability of the mixed perovskite phases compared to the pure phases using the mixing free energy, $\Delta F_{phase} = \Delta E_{phase} - T\Delta S_{phase}$, which accounts for both energetic and entropic contributions to measure the thermodynamic compatibility of FMA^+ and FA^+ (Figure 1e). The energetic contribution was calculated using DFT as:

$$\Delta E_{phase}(FMA_xFA_{1-x}PbI_3) = E_{phase}(FMA_xFA_{1-x}PbI_3) - \left[xE_{phase}(FMAPbI_3) + (1-x)E_{phase}(FAPbI_3)\right]$$

where $E_{phase}(FMA_xFA_{1-x}PbI_3)$, $E_{phase}(FMAPbI_3)$, and $E_{phase}(FAPbI_3)$, and E_{PbI_2} are the total energies of the mixed perovskite composition and of the FMA- and FA-pure perovskites, and x represents the molar fraction of FMA^+ incorporated into the $FAPbI_3$ lattice. The entropic contribution was estimated using the ideal-alloy approximation [56]:

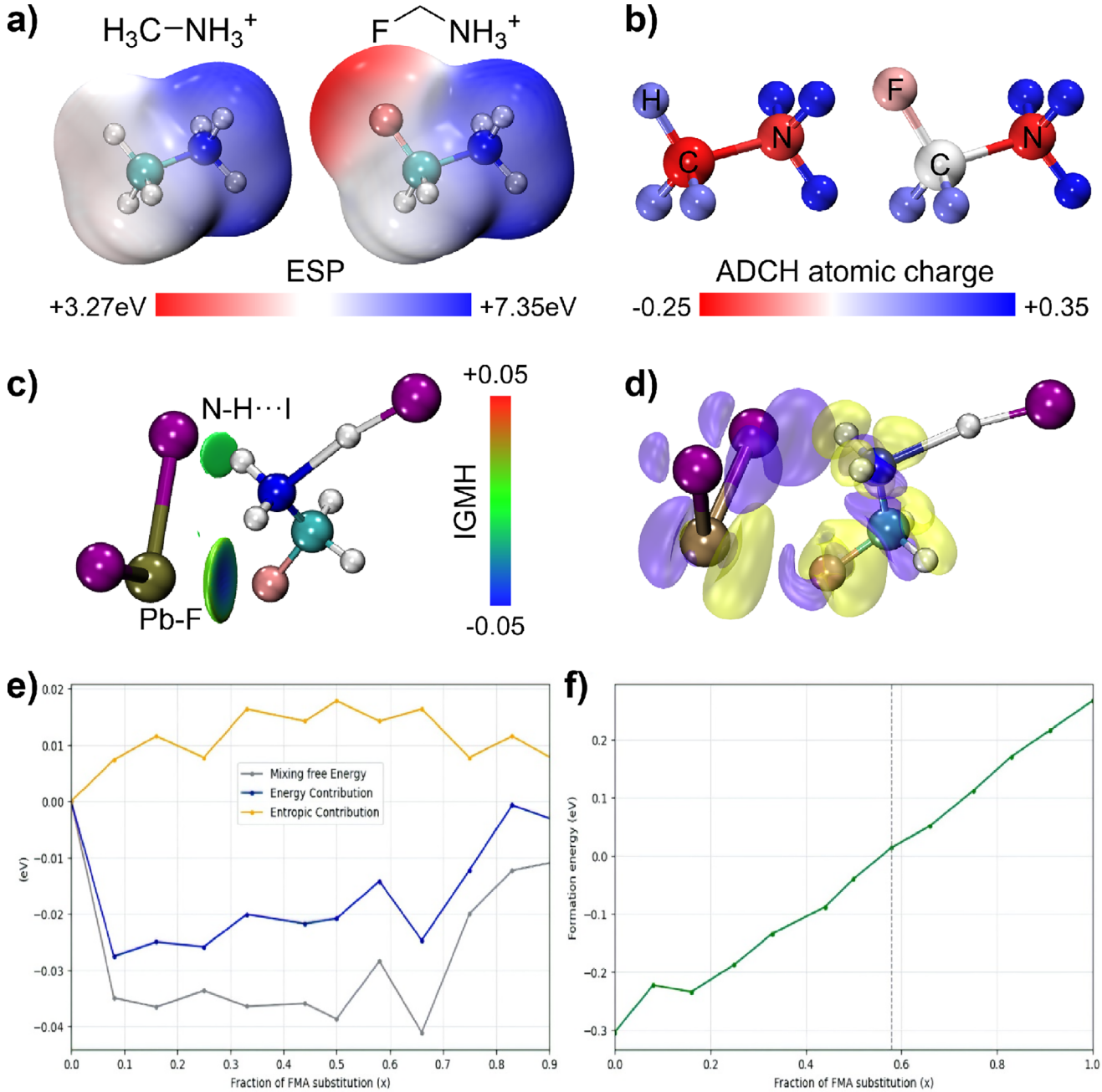

FIGURE 1 | (a) Results of isolated molecule calculations: Electrostatic surface potential (ESP) maps of MA^+ and FMA^+. (b) Atomic dipole corrected Hirshfeld (ADCH) atomic charge of MA^+ and FMA^+. (c) Independent gradient model based on Hirshfeld partition of molecular density (IGMH) analysis of the interaction between FMAI and PbI_2, shown at an isovalue of 0.01 a.u. (d) Electron density difference map of a FMAI-PbI_2 complex. Purple and yellow regions indicate electron accumulation and depletion, respectively. The isovalue is 0.001 a.u. (e) Results of periodic calculations for the crystalline system: Mixing free energy as a function of FMA^+ concentration, including the corresponding enthalpic and entropic contributions. (f) Formation energy of $FMA_xFA_{1-x}PbI_3$ as a function of FMA^+ concentration. Note that the vertical axis shows the change in formation energy relative to the pristine phase. The dashed line indicates the composition at which the calculated formation energy changes sign.

$$\Delta S_{\text{phase}}\left(FMA_xFA_{1-x}PbI_3\right) = -k_B\left[xln\left(x\right) + \left(1-x\right)ln\left(1-x\right)\right]$$

where k_B is the Boltzmann constant and x represents the molar fraction of FMA^+ incorporated into the $FAPbI_3$ lattice. The differences among the calculated $\Delta E_{\text{phase}}(FMA_xFA_{1-x}PbI_3)$ energies are small, approximately 0.01 eV per stoichiometric unit, indicating that replacing FA^+ with FMA^+ does not introduce a large enthalpic penalty. The entropic contribution $-T\Delta S_{\text{phase}}$ is negative and therefore favors cation mixing, with the maximum stabilization at $x = 0.5$. As shown in Figure 1e, the resulting ΔF_{phase} is thermodynamically favorable over the modeled range, suggesting that FA^+ and FMA^+ are compatible within the same perovskite phase, suggesting that once the perovskite is formed, the components are likely to remain mixed rather than segregating. In contrast, the formation energy at high doping concentration indicates that high FMA^+ fractions become increasingly unfavorable relative to the precursor phases.

To study the molecular properties of FMAI and its possible interactions with perovskite-related species, we performed isolated molecular DFT calculations [57–59]. Electrostatic surface potential (ESP) maps (Figure 1a) confirmed that the electron-withdrawing nature of the F atom leads to a larger dipole moment (μ) of FMA^+ (5.90 D) and an increased difference ($\Delta\varphi$) in the ESP (4.27 eV) (Figures S2 and S3), compared to MA^+ (2.19 D and 2.34 eV, respectively). Atomic dipole corrected Hirshfeld (ADCH) charge analysis (Figure 1b) shows an overaccumulation of negative charge over the fluorine site in FMA^+ with respect to the analogous proton in MA^+ (0.072 for F in FMA^+ vs. +0.170 for H in MA^+). This excess polarity in the partly negatively charged fluorine atom enables binding with Pb^{2+}, which establishes Lewis acid–base interactions, as observed in the independent gradient model based on Hirshfeld partition of molecular density (IGMH) maps, electron density differences, and topology analyses on electron density (Figure 1c,d and Figures S4 and S5) [60, 61]. FMAI transfers electrons to PbI_2 while MAI accepts electrons from PbI_2 (Figure S5). Additionally, according to the DFT calculation, the positively charged NH_3^+ fragment can establish hydrogen bonds with the iodide atoms in its proximity. Overall, the binding energy of FMAI-PbI_2 is −0.63 eV compared to 0.36 eV for MAI-PbI_2. These interactions could lead to the passivation of iodide vacancy (V_I) and coordination of undercoordinated Pb^{2+} in the perovskite film [60, 61].

We have recently shown that perovskite additives are sometimes non-innocent and participate in beneficial reactivity within the perovskite system [61]. Given the known lability of α-fluorinated ammonium salts [51–53], we also considered whether FMAI may not exclusively act as an A-site cation, but additionally as a reactive additive. The NMR spectra of freshly prepared FMAI exhibit the expected ^1H, ^{13}C, and ^{19}F NMR resonances, confirming formation of the target fluoromethylammonium iodide salt (Figure S1). However, time-dependent ^{19}F NMR spectroscopy measurements in d_6-DMSO over 128 h at 25°C revealed the growth of additional fluorine-containing species (Figure S6) with features at −140 ppm (dd, J = 35.0, 17.3 Hz), at −148 ppm (singlet), and at −150 ppm (broad), ascribed to an unknown potentially fluorocarbon product, to HF_2^- [56], and to potentially fluorinated glass (from the NMR spectroscopy tube) [54], respectively. The latter two species likely arise from released F^- and HF from the 1,2-elimination reaction in FMAI (Figure S6). No changes were observed in the corresponding time-dependent ^1H NMR spectra (Figure S7), except for a slight shift and broadening of the ammonium proton resonance from 7.04 to 6.42 ppm, with no substantial changes to the integration or relative ratios. This suggests that the reactivity is slow in the precursor solution (liquid state) and would be even slower in the films (solid). After several weeks, colorless single crystals were observed in the NMR spectroscopy tubes, which were collected and analyzed. Single-crystal X-ray diffraction identified the presence of two ionic molecules in the structure: a protonated hexamethylenetetramonium (HMTA) and an ammonium (NH_4^+) cation with the corresponding iodide anions (Figure S8). The formation of this species indicates that FMAI reactivity not only generates fluorine- and fluoride-containing byproducts, but also produces reactive C/N-containing fragments that can undergo condensation reactions. HMTA is classically prepared by condensation of formaldehyde with ammonia or ammonium-derived species, via a reactive methanimine intermediate. The crystallographic identification of a HMTA salt in the crystal could be consistent with the generation of such species during the slow FMAI reactivity likely via a 1,2-elimination of HF (Figure S9). HMTA has been previously shown to be beneficial in PSCs by enhancing the α-phase stability of $FAPbI_3$ [62] and the presence of HI and HF can increase the stability of the perovskite precursor solutions [63], and can lead to PSCs with higher PCE through doping and passivation [64, 65]. Although the complementary crystal structure and NMR spectroscopy data do not establish the complete reactivity pathway, it provides evidence that FMAI might be chemically non-innocent in the perovskite.

We next investigated the effect of incorporating FMAI into perovskite films and PSCs (full preparation details are given in the Supporting Information) fabricated from solutions of the generic form $Cs_{0.06}FA_{0.94}Pb(I_{1-x}Cl_x)_3$. Films and devices without FMAI are referred to as Control, whereas those incorporating 0.8 mol% FMAI (relative to the total amount of CsCl and FAI), the optimized FMAI concentration (Table S2 and Figure S16) based on overall performance, are referred to as Target.

The powder X-ray diffraction (pXRD) patterns of the fresh (t = 0 days) Target perovskite films exhibit the typical perovskite peak at ∼14° (Figure 2), without any additional peaks observed due to the addition of FMAI. The presence of FMAI in the Target perovskite film, however, suppresses decomposition, as much less residual PbI_2 is generated compared to the Control samples during thermal aging (60°C in N_2) evidenced by the peak at ∼12.5° (Figure 2a). In addition, the Target film does not exhibit the photoinactive hexagonal $FAPbI_3$ δ-phase (yellow phase) peak at ∼12° during moisture aging (30%–40% RH at room temperature), even after 30 days, indicating that the FMA^+ cation stabilizes the black phase of perovskite (Figure 2b).

Scanning electron microscopy (SEM) was used to further investigate the perovskite film structure. The addition of 0.8 mol% FMAI improves the Target film quality with larger grains and a smoother, more compact surface morphology observed in the top-view images compared to the Control film (Figure 3a). After both thermal and moisture aging, the Target films containing FMAI continue to exhibit a denser perovskite surface with fewer voids than the Control (Figures S10 and S11). Cross-sectional SEM images of devices show the expected glass, FTO, TiO_2, perovskite, HTL, and gold electrode layers. Partial delamination of the gold electrode occurred during device fracture, but the main device layers remained identifiable. The Control perovskite layer showed limited through-thickness texturing, whereas the Target film appeared more compact, although the apparent crystal size in the bulk differed from the surface morphology (Figure S12). We next performed X-ray photoelectron spectroscopy (XPS) measurements to experimentally probe the interaction between F and Pb. Specifically, the Pb 4f spectrum exhibits a clear shift toward lower binding energy (by ∼0.3 eV) upon introduction of FMAI, which is consistent with Pb–F interaction as previously evidenced by DFT calculations (Figure S17).

The photophysical properties and carrier dynamics of the Control and Target films were evaluated using relative photoluminescence (PL) intensity and voltage-dependent transient PL decay measurements (Figure 3b,c). The Target film shows higher PL intensity and longer PL decay lifetime (728 ns vs 245 ns,

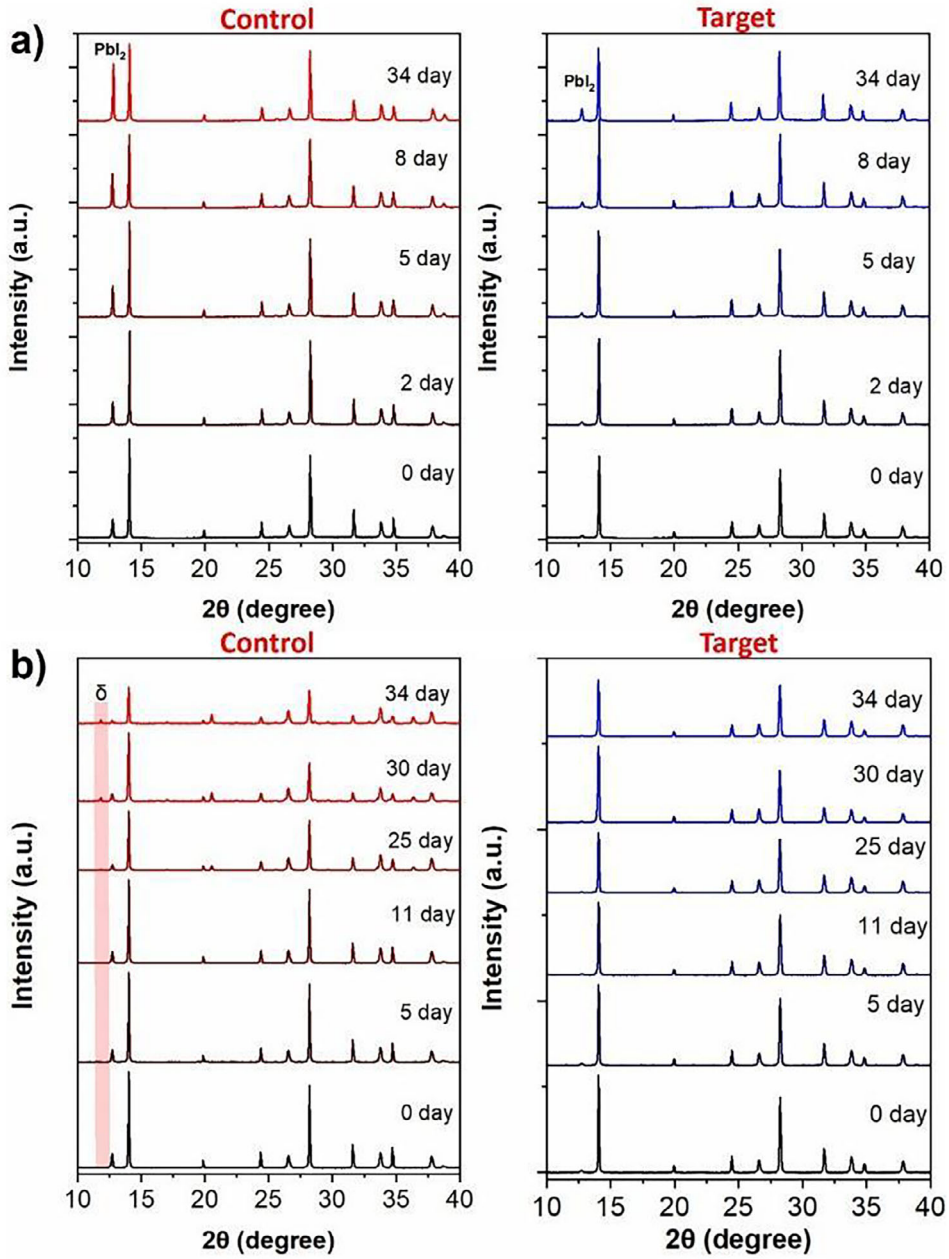

FIGURE 2 | XRD patterns of Control and Target perovskite films during (a) thermal aging at 60°C in N_2 glove box; (b) moisture aging under 30%–40% RH at room temperature.

respectively) than the Control film, reduced non-radiative recombination and grain boundary defect passivation. The PL decay profiles of the Control can be fitted to a biexponential containing a fast component, associated with defects- or impurity-induced recombination, and a slower component arising from radiative recombination occurring in the bulk perovskite. In contrast, the Target exhibits a more gradual decay, consistent with reduced trap recombination. Confocal PL mapping further confirms that the Target perovskite films exhibit higher PL intensity and a narrower emission wavelength distribution than the Control films (Figure 3d,e). These differences are consistent with the enhanced film uniformity and defect passivation, presumably arising from interactions between FMAI and undercoordinated Pb^{2+} or iodine vacancies. The absorption spectra of the Control and Target films, consistent with the External Quantum Efficiency (EQE) response (Figure 4b), exhibit a similar absorption onset around 750 nm (Figure S13), indicating that the low FMAI loading does not significantly alter the optical bandgap of the perovskite.

The performance of the Control and Target PSCs was evaluated using devices based on architectures comprising FTO/TiO_2/SnO_2/perovskite/PMMA/Spiro-OMeTAD:PDCBT/Au. The statistical performance of the devices is shown in Figure 4 and Table 1. The performance improvement in the Target PSCs primarily arises from increased V_{OC} and FF, which benefit from the reduced non-radiative recombination, improved charge extraction, and defect passivation effect of FMAI discussed above, while the J_{SC} remains essentially unchanged within experimental deviation. The champion Target PSC showed $J_{SC} = 26.67\ mA/cm^2$, $V_{OC} = 1.15$ V, and FF = 83.9%, which resulted in an overall PCE

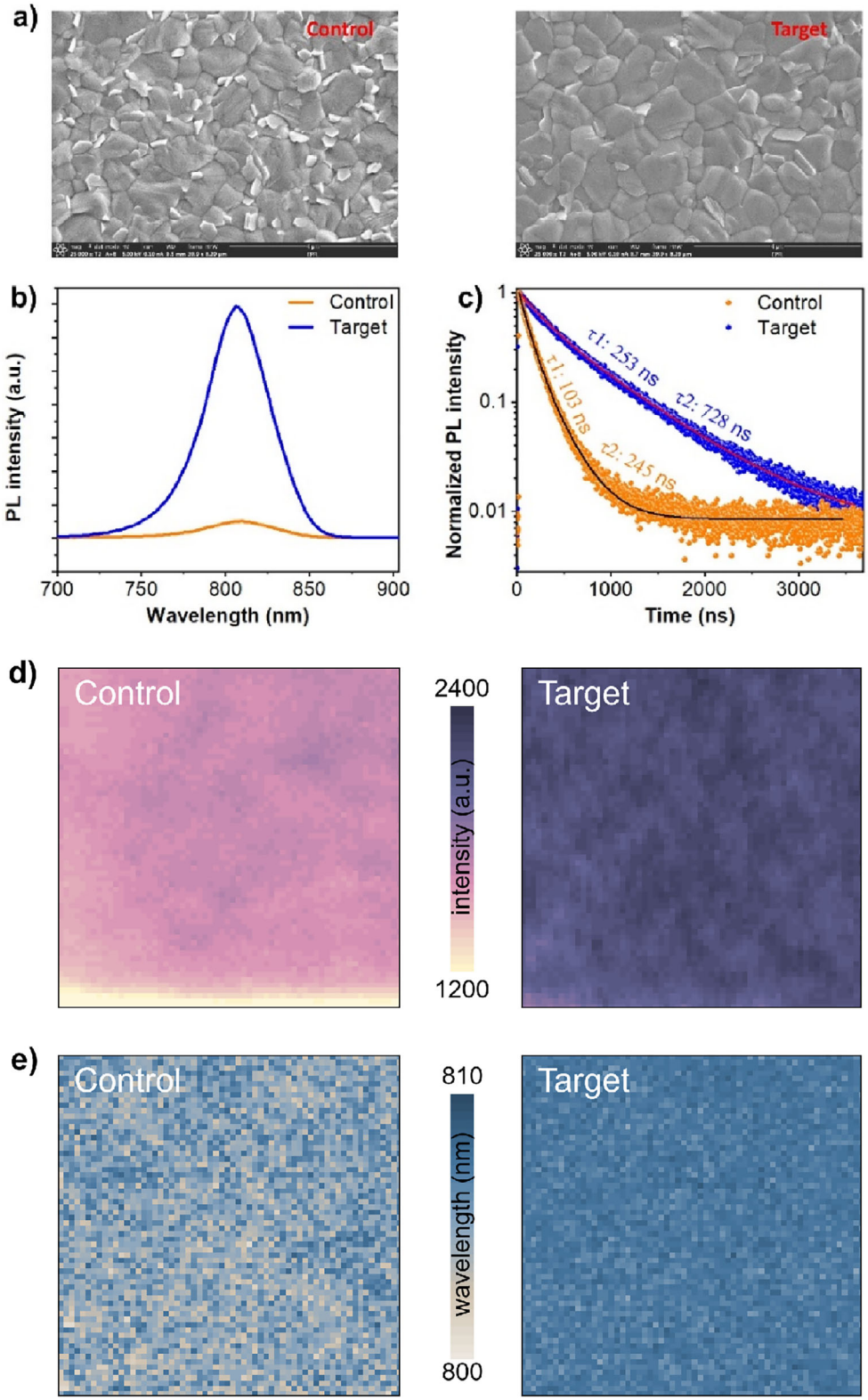

FIGURE 3 | (a) Top-view SEM images; (b) PL spectra; and (c) voltage-dependent transient PL decay lifetime of the Control and Target perovskite films. Mapping of (d) PL intensity and (e) wavelength of the Control and Target perovskite films. Data were obtained over an area of 43 μm × 43 μm.

of 25.67% with small hysteresis (Figure 4a). In comparison, the Control PSC showed J_{SC} = 26.51 mA/cm^2, V_{OC} = 1.10 V, and FF = 81.8%, corresponding to a PCE of 23.87%. The stabilized power output under maximum power point tracking reached 25.38% (Figure 4a, inset), which is in good agreement with the *J*–*V* scans. Statistical analysis of more than 30 devices confirms the reproducibility of the performance improvement in the Target PSCs (Figure 4c–f). shows statistically relevant improvements in the performance of over 30 PSCs. The PCE values obtained here are highly competitive for FA/Cs-based single-junction PSCs

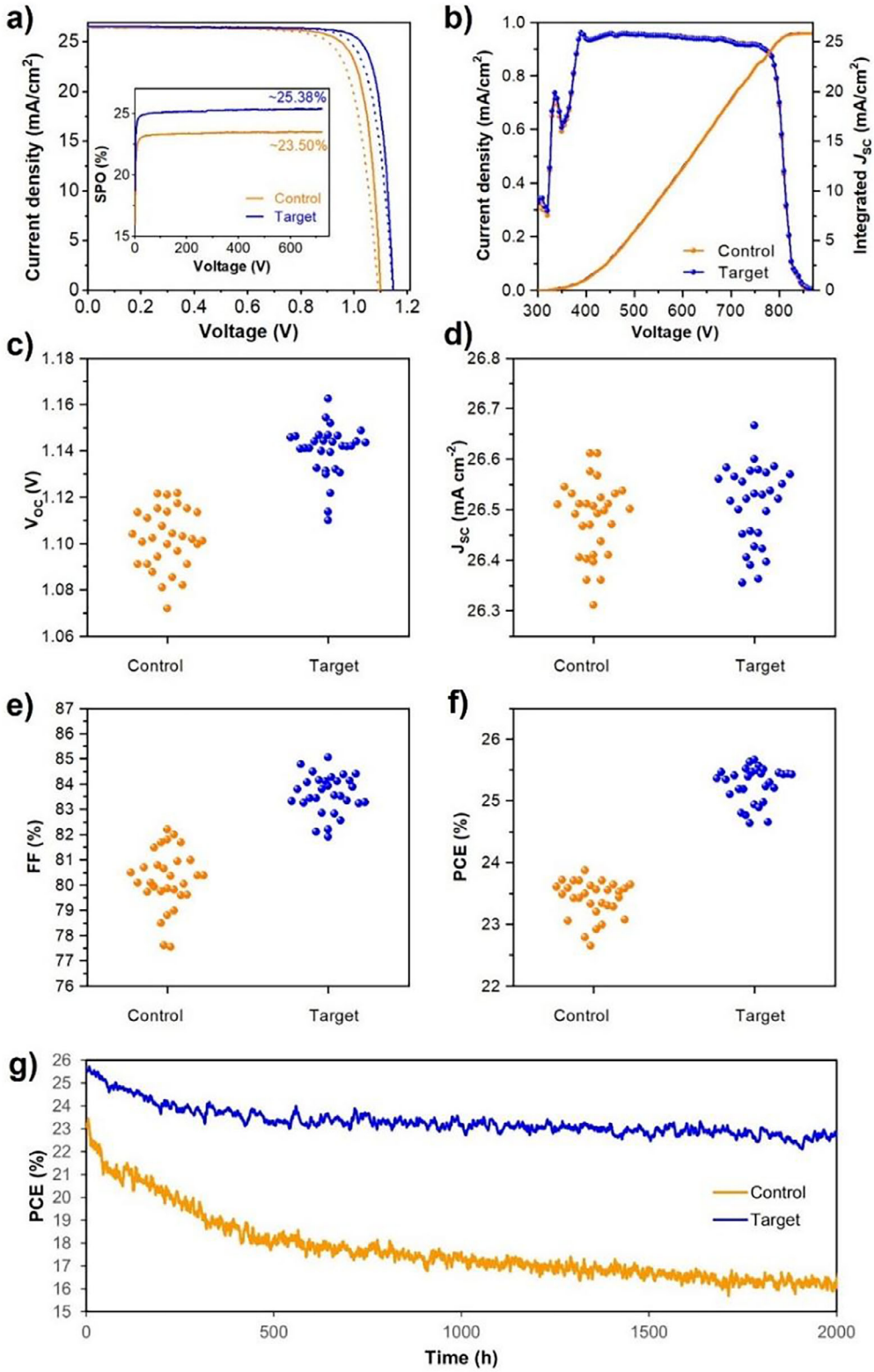

FIGURE 4 | (a) Current–voltage scans for the best performing Control and Target devices showing the entire hysteresis loop and maximum power point tracking (inset); (b) external quantum efficiency spectra and integrated short-circuit current density of the corresponding devices; statistics of the photovoltaic parameters (c) V_{OC}, (d) J_{SC}, (e) FF, and (f) PCE of Control and Target devices ($n \geq 30$); (g) maximum power point (MPP) tracking for 2000 h of the encapsulated devices under continuous light (100 mW cm^{-2}) illumination at 25°C in a nitrogen atmosphere.

TABLE 1 | Summary of the best and average device performance for the Control and Target devices with the statistical standard deviation of parameter distribution from 30 samples for each condition.

	V_{OC} (V)	J_{SC} (mA cm^{-2})	FF (%)	PCE (%)
Control	1.10 ± 0.01	26.48 ± 0.07	80.22 ± 1.17	23.41 ± 0.30
Best	1.10	26.51	81.80	23.87
Target	1.14 ± 0.01	26.51 ± 0.08	83.60 ± 0.78	25.26 ± 0.29
Best	1.15	26.67	83.93	25.67

prepared using low-concentration molecular additives, confirming the potential of the fluorinated FMA^+ cation to improve photovoltaic performance.

The operational stability of encapsulated devices was evaluated under maximum power point (MPP) tracking under simulated solar illumination, following an ISOS-L-1 protocol as established by the International Summits on Organic Photovoltaic Stability [66]. The light-soaking performance of the encapsulated PSCs was evaluated under 1 sun illumination under an inert atmosphere. The Target PSC retained ~88% of its original PCE after 2000 h, compared to ~70% for the Control PSCs under the same conditions. These results demonstrate that the incorporation of FMAI improves both the initial device performance, as well as the operational stability.

To evaluate the broader applicability of the FMAI treatment, we further tested the additive in perovskite formulations with different bandgaps and in mini-module devices. Target devices based on 1.60, 1.65, and 1.75 eV perovskite absorbers showed improved photovoltaic performance compared to the corresponding Control devices (Figure S15), indicating that the beneficial effect of FMAI is not limited to a single perovskite composition. To assess scalability, we fabricated an FMAI-containing perovskite mini-module with a total active area of 29 cm^2 (Figure S14). The module was completed by laser etching and contained nine subcells connected in series. Encouragingly, the Target module exhibited a V_{OC} of 10.19 V, a J_{SC} of 75.84 mA, an FF of 78.1%, and a PCE of 20.76%. The high module performance originates from the good uniformity of the perovskite layer, the reduced trap density, and suppressed interfacial recombination, supporting the potential of FMAI for scalable fabrication of PSCs.

3 | Conclusions

Fluoromethylammonium iodide (FMAI) was employed as a low-concentration additive for FA/Cs-based perovskite films, motivated by its potential 3D perovskite doping and defect-passivation interactions. Perovskite films with 0.8 mol% FMAI, i.e., Target films, comprise larger and smoother grains and exhibit superior relative PL intensity and PL decay lifetime compared to the Control film, i.e., without FMAI. The n-i-p PSCs fabricated with the Target perovskite films achieve a PCE of 25.67% and long-term operational stability for 2000 h. Hence, the new FMA^+ cation, which may be prepared using a facile procedure, is expected to find widespread applications in the design of next-generation perovskite-based photovoltaics, light-emitting diodes, sensors, and beyond.

Author Contributions

Justina Mikuciunaite: investigation, data curation. **Vytautas Getautis**: project administration, resources. **Kasparas Rakstys**: conceptualization, writing – review and editing, writing – original draft, supervision, project administration. **Yong Ding**: data curation, validation. **Lindsey E. K. Frederiksen**: methodology, formal analysis. **Yuxuan Yang**: methodology, validation. **Yi Zhang**: supervision, writing – review and editing. **Xiao-Xin Gao**: formal analysis, validation. **Farzaneh Fadaei Tirani**: data curation, investigation. **Mohammad Khaja Nazeeruddin**: supervision, writing – review and editing. **Bin Ding**: conceptualization, methodology. **Jan Romano-degea**: validation, conceptualization. **Negar Ashari Astani**: writing – review and editing, supervision. **Vida Valipour**: software, data curation.

Acknowledgements

J.M., B.D., and Y.Y. contributed equally to this work. Funded by the European Union. Views and opinions expressed are however, those of the author(s) only and do not necessarily reflect those of the European Union or the European Climate, Infrastructure and Environment Executive Agency. Neither the European Union nor the granting authority can be held responsible for them. HEPAFLEX project has received funding from HORIZON Research and Innovation Actions under Grant Agreement no. 101122345. This work was also supported by the Research Council of Lithuania via grant No. S-MIP-20-20 and received partial funding from a research grant "Leading House South Asia and Iran, Zurich University of Applied Sciences" between EPFL and Amirkabir University of Technology. K.R. thanks the funding from the World Federation of Scientists (WFS) fellowship and the Lithuanian Academy of Sciences Young Researcher scholarship. We thank Prof. Paul J. Dyson (EPFL) for providing infrastructure, obtaining and providing financial support, extensive discussions, critical feedback, and editing the manuscript and supporting information. We also thank the EPFL for financial support and Dr. L. A. Phroaig for the fruitful discussions. We appreciate Dr. Tian Lu at Beijing Kein Research Center for Natural Sciences for the free programs, including Multiwfn for comprehensive and splendid wave function analyses (http://sobereva.com/multiwfn/).

Conflicts of Interest

The authors declare no conflicts of interest.

Data Availability Statement

The data that support the findings of this study are available from the corresponding author upon reasonable request.

References

1. A. Kojima, K. Teshima, Y. Shirai, and T. Miyasaka, "Organometal Halide Perovskites as Visible-Light Sensitizers for Photovoltaic Cells," *Journal of the American Chemical Society* 131 (2009): 6050–6051, https://doi.org/10.1021/ja809598r.

2. J. Burschka, N. Pellet, and S. J. Moon, "Sequential Deposition as a Route to High-Performance Perovskite-Sensitized Solar Cells," *Nature* 499 (2013): 316–319, https://doi.org/10.1038/nature12340.

3. H. S. Kim, C. R. Lee, J. H. Im, et al., "Lead Iodide Perovskite Sensitized All-Solid-State Submicron Thin Film Mesoscopic Solar Cell With Efficiency Exceeding 9%," *Scientific Reports* 2 (2012): 591, https://doi.org/10.1038/srep00591.

4. J. Y. Kim, J. W. Lee, H. S. Jung, H. Shin, and N. G. Park, "High-Efficiency Perovskite Solar Cells," *Chemical Reviews* 120 (2020): 7867–7918, https://doi.org/10.1021/acs.chemrev.0c00107.

5. Z. K. Tan, R. S. Moghaddam, M. L. Lai, et al., "Bright Light-Emitting Diodes Based on Organometal Halide Perovskite," *Nature Nanotechnology* 9 (2014): 687–692, https://doi.org/10.1038/nnano.2014.149.

6. G. Pacchioni, "Highly Efficient Perovskite LEDs," *Nature Reviews Materials* 6 (2021): 108, https://doi.org/10.1038/s41578-021-00280-5.

7. S. D. Stranks and H. J. Snaith, "Metal-Halide Perovskites for Photovoltaic and Light-Emitting Devices," *Nature Nanotechnology* 10 (2015): 391–402, https://doi.org/10.1038/nnano.2015.90.

8. G. Xing, N. Mathews, S. S. Lim, et al., "Low-Temperature Solution-Processed Wavelength-Tunable Perovskites for Lasing," *Nature Materials* 13 (2014): 476–480, https://doi.org/10.1038/nmat3911.

9. Q. Zhang, Q. Shang, R. Su, T. T. H. Do, and Q. Xiong, "Halide Perovskite Semiconductor Lasers: Materials, Cavity Design, and Low Threshold," *Nano Letters* 21 (2021): 1903–1914, https://doi.org/10.1021/acs.nanolett.0c03593.

10. H. Wang and D. H. Kim, "Perovskite-Based Photodetectors: Materials and Devices," *Chemical Society Reviews* 46 (2017): 5204–5236, https://doi.org/10.1039/C6CS00896H.

11. F. Liu, R. Wu, J. Wei, et al., "Recent Progress in Halide Perovskite Radiation Detectors for Gamma-Ray Spectroscopy," *ACS Energy Letters* 7 (2022): 1066–1085, https://doi.org/10.1021/acsenergylett.2c00031.

12. P. V. Shinde, A. Patra, and C. S. Rout, "A Review on the Sensing Mechanisms and Recent Developments on Metal Halide-Based Perovskite Gas Sensors," *Journal of Materials Chemistry C* 10 (2022): 10196–10223, https://doi.org/10.1039/D2TC01980A.

13. M. J. Seol, S. H. Hwang, J. W. Han, H. W. Jang, and S. Y. Kim, "Recent Progress of Halide Perovskites Applied to Five Senses Sensors," *ACS Applied Electronic Materials* 5 (2022): 5261–5277, https://doi.org/10.1021/acsaelm.2c01329.

14. "Best Research-Cell Efficiency Chart | Photovoltaic Research | NREL," https://www.nrel.gov/pv/cell-efficiency.html.

15. L. Meng, J. You, and Y. Yang, "Addressing the Stability Issue of Perovskite Solar Cells for Commercial Applications," *Nature Communications* 9 (2018): 5265.

16. J. M. Ball and A. Petrozza, "Defects in Perovskite-Halides and Their Effects in Solar Cells," *Nature Energy* 1 (2016): 16149, https://doi.org/10.1038/nenergy.2016.149.

17. T. J. Jacobsson, J. P. Correa-Baena, et al., E. Halvani Anaraki, "Unreacted PbI_2 as a Double-Edged Sword for Enhancing the Performance of Perovskite Solar Cells," *Journal of the American Chemical Society* 138 (2016): 10331–10343, https://doi.org/10.1021/jacs.6b06320.

18. Q. Jiang, Z. Chu, P. Wang, et al., "Planar-Structure Perovskite Solar Cells With Efficiency Beyond 21%," *Advanced Materials* 29 (2017): 1703852, https://doi.org/10.1002/adma.201703852.

19. Y. H. Lin, N. Sakai, P. Da, et al., "A Piperidinium Salt Stabilizes Efficient Metal-Halide Perovskite Solar Cells," *Science* 369 (2020): 96–102, https://doi.org/10.1126/science.aba1628.

20. X. Wang, K. Rakstys, K. Jack, et al., "Engineering Fluorinated-Cation Containing Inverted Perovskite Solar Cells With an Efficiency of> 21% and Improved Stability Towards Humidity," *Nature Communications* 12 (2021): 52.

21. M. Saliba, T. Matsui, J. Y. Seo, et al., "Cesium-Containing Triple Cation Perovskite Solar Cells: Improved Stability, Reproducibility and High Efficiency," *Energy & Environmental Science* 9 (2016): 1989–1997, https://doi.org/10.1039/C5EE03874J.

22. N. Pellet, P. Gao, G. Gregori, et al., "Mixed-Organic-Cation Perovskite Photovoltaics for Enhanced Solar-Light Harvesting," *Angewandte Chemie International Edition* 53 (2014): 3151–3157, https://doi.org/10.1002/anie.201309361.

23. J. W. Lee, S. Tan, S. Il Seok, Y. Yang, and N. G. Park, "Rethinking the A Cation in Halide Perovskites," *Science* 375 (2022): abj1186, https://doi.org/10.1126/science.abj1186.

24. M. M. Byranvand, C. Otero-Martínez, J. Ye, et al., "Recent Progress in Mixed A-Site Cation Halide Perovskite Thin-Films and Nanocrystals for Solar Cells and Light-Emitting Diodes," *Advanced Optical Materials* 10 (2022): 2200423, https://doi.org/10.1002/adom.202200423.

25. S. H. Turren-Cruz, A. Hagfeldt, M. Saliba, et al., "Methylammonium-Free, High-Performance, and Stable Perovskite Solar Cells on a Planar Architecture," *Science* 362 (2018): 449–453, https://doi.org/10.1126/science.aat3583.

26. K. Wang, J. Huo, L. Cao, et al., "Fully Methylammonium-Free Stable Formamidinium Lead Iodide Perovskite Solar Cells Processed Under Humid Air Conditions," *ACS Applied Materials & Interfaces* 15 (2023): 13353–13362, https://doi.org/10.1021/acsami.2c23134.

27. Y. Bekenstein, B. A. Koscher, S. W. Eaton, P. Yang, and A. P. Alivisatos, "Highly Luminescent Colloidal Nanoplates of Perovskite Cesium Lead Halide and Their Oriented Assemblies," *Journal of the American Chemical Society* 137 (2015): 16008–16011, https://doi.org/10.1021/jacs.5b11199.

28. N. J. Jeon, J. H. Noh, W. S. Yang, et al., "Compositional Engineering of Perovskite Materials for High-Performance Solar Cells," *Nature* 517 (2015): 476–480, https://doi.org/10.1038/nature14133.

29. G. E. Eperon, S. D. Stranks, C. Menelaou, M. B. Johnston, L. M. Herz, and H. J. Snaith, "Formamidinium Lead Trihalide: A Broadly Tunable Perovskite for Efficient Planar Heterojunction Solar Cells," *Energy & Environmental Science* 7 (2014): 982, https://doi.org/10.1039/c3ee43822h.

30. C. C. Stoumpos, C. D. Malliakas, and M. G. Kanatzidis, "Semiconducting Tin and Lead Iodide Perovskites With Organic Cations: Phase Transitions, High Mobilities, and Near-Infrared Photoluminescent Properties," *Inorganic Chemistry* 52 (2013): 9019–9038, https://doi.org/10.1021/ic401215x.

31. E. T. Hoke, D. J. Slotcavage, E. R. Dohner, A. R. Bowring, H. I. Karunadasa, and M. D. McGehee, "Reversible Photo-Induced Trap Formation in Mixed-Halide Hybrid Perovskites for Photovoltaics," *Chemical Science* 6 (2015): 613–617, https://doi.org/10.1039/C4SC03141E.

32. B. Conings, J. Drijkoningen, N. Gauquelin, et al., "Intrinsic Thermal Instability of Methylammonium Lead Trihalide Perovskite," *Advanced Energy Materials* 5 (2015): 1500477, https://doi.org/10.1002/aenm.201500477.

33. J. H. Noh, S. H. Im, J. H. Heo, T. N. Mandal, and S. I. Seok, "Chemical Management for Colorful, Efficient, and Stable Inorganic–Organic Hybrid Nanostructured Solar Cells," *Nano Letters* 13 (2013): 1764–1769, https://doi.org/10.1021/nl400349b.

34. Y. Bai, Z. Huang, X. Zhang, et al., "Initializing Film Homogeneity to Retard Phase Segregation for Stable Perovskite Solar Cells," *Science* 378 (2022): 747–754, https://doi.org/10.1126/science.abn3148.

35. M. Abdi-Jalebi, Z. Andaji-Garmaroudi, S. Cacovich, et al., "Maximizing and Stabilizing Luminescence From Halide Perovskites With Potassium Passivation," *Nature* 555 (2018): 497–501, https://doi.org/10.1038/nature25989.

36. M. Saliba, T. Matsui, K. Domanski, et al., "Incorporation of Rubidium Cations into Perovskite Solar Cells Improves Photovoltaic Performance," *Science* 354 (2016): 206–209, https://doi.org/10.1126/science.aah5557.

37. M. A. Mahmud, T. Duong, J. Peng, et al., "Origin of Efficiency and Stability Enhancement in High-Performing Mixed Dimensional 2D-3D

Perovskite Solar Cells: A Review," *Advanced Functional Materials* 32 (2022): 2009164, https://doi.org/10.1002/adfm.202009164.

38. G. Liu, X. X. Xu, S. Xu, et al., "Passivation Effect of Halogenated Benzylammonium as a Second Spacer Cation for Improved Photovoltaic Performance of Quasi-2D Perovskite Solar Cells," *Journal of Materials Chemistry A* 8 (2020): 5900–5906, https://doi.org/10.1039/C9TA14139A.

39. T. Zhao, C. C. Chueh, Q. Chen, A. Rajagopal, and A. K. Y. Jen, "Defect Passivation of Organic–Inorganic Hybrid Perovskites by Diammonium Iodide Toward High-Performance Photovoltaic Devices," *ACS Energy Letters* 1 (2016): 757–763, https://doi.org/10.1021/acsenergylett.6b00327.

40. G. Grancini, C. Roldán-Carmona, I. Zimmermann, et al., "One-Year Stable Perovskite Solar Cells by 2D/3D Interface Engineering," *Nature Communications* 8 (2017): 15684, https://doi.org/10.1038/ncomms15684.

41. A. Bala and V. Kumar, "Fluorinated 2-Phenylethylammonium Spacer Cations for Improved Stability of Ruddlesden–Popper Pb/Sn Halide Perovskites: Insight From First-Principles Calculations," *ACS Applied Energy Materials* 6 (2023): 5710.

42. G. Yan, G. Sui, W. Chen, K. Su, Y. Feng, and B. Zhang, "Selectively Fluorinated Benzylammonium-Based Spacer Cation Enables Graded Quasi-2D Perovskites for Efficient and Stable Solar Cells," *Chemistry of Materials* 34 (2022): 3346–3356, https://doi.org/10.1021/acs.chemmater.2c00146.

43. L. Wang, Q. Zhou, Z. Zhang, et al., "A Guide to Use Fluorinated Aromatic Bulky Cations for Stable and High-Performance 2D/3D Perovskite Solar Cells: The More Fluorination the Better?," *Journal of Energy Chemistry* 64 (2022): 179–189, https://doi.org/10.1016/j.jechem.2021.04.063.

44. Q. Zhou, Q. Xiong, Z. Zhang, et al., "Toward Efficient and Stable Perovskite Solar Cells: Choosing Appropriate Passivator to Specific Defects," *Solar RRL* 4 (2020): 2070104, https://doi.org/10.1002/solr.202000107.

45. X. Meng, R. Zhang, Z. Fu, and Q. Zhang, "Domain—Dependent Electronic Structure and Optical Absorption Property in Hybrid Organic–inorganic Perovskite," *Physical Chemistry Chemical Physics* 18 (2016): 27358–27365, https://doi.org/10.1039/C6CP03377F.

46. A. Laref, M. Al-Enazi, H. R. Al-Qahtani, S. Laref, and X. Wu, "Impact of Fluorine on Organic Cation for Determining the Electronic and Optical Properties of $CH_{3-x}F_xNH_3PbI_3$ (x = 0, 1, 2, 3) Hybrid Perovskites-Based Photovoltaic Devices," *Solar Energy* 177 (2019): 517–530, https://doi.org/10.1016/j.solener.2018.11.026.

47. I. Alkorta and J. Elguero, "A Theoretical Study of Perovskites Related to $CH_3NH_3PbX_3$ (X = F, Cl, Br, I)," *New Journal of Chemistry* 42 (2018): 13889–13898, https://doi.org/10.1039/C8NJ01879K.

48. J. M. Frost, K. T. Butler, F. Brivio, C. H. Hendon, M. Van Schilfgaarde, and A. Walsh, "Atomistic Origins of High-Performance in Hybrid Halide Perovskite Solar Cells," *Nano Letters* 14 (2014): 2584–2590, https://doi.org/10.1021/nl500390f.

49. S. Huang, P. Huang, L. Wang, J. Han, Y. Chen, and H. Zhong, "Halogenated-Methylammonium Based 3D Halide Perovskites," *Advanced Materials* 31 (2019): 1903830, https://doi.org/10.1002/adma.201903830.

50. C. Li, X. Lu, W. Ding, L. Feng, Y. Gao, and Z. Guo, "Formability of ABX_3 (X = F, Cl, Br, I) Halide Perovskites," *Acta Crystallographica Section B Structural Science* 64 (2008): 702–707, https://doi.org/10.1107/S0108768108032734.

51. L. Radom, W. J. Hehre, and J. A. Pople, "Molecular Orbital Theory of the Electronic Structure of Organic Compounds. VIII. Geometries, Energies, and Polarities of C3 Hydrocarbons," *Journal of the American Chemical Society* 93 (1971): 5339–5342, https://doi.org/10.1021/ja00750a005.

52. W. Leidinger and W. Sundermeyer, "Zur Chemie des (Trifluormethyl)Sulfinylamins, CF_3 NSO, und Verwandter Verbindungen," *Chemische Berichte* 115 (1982): 2892–2897, https://doi.org/10.1002/cber.19821150819.

53. G. Klöter, W. Lutz, K. Seppelt, and W. Sundermeyer, "Trifluoromethylamine, CF_3NH_2," *Angewandte Chemie International Edition in English* 16 (1977): 707–708.

54. R. E. Youngman and S. Sen, "The Nature of Fluorine in Amorphous Silica," *Journal of Non-Crystalline Solids* 337 (2004): 182–186, https://doi.org/10.1016/j.jnoncrysol.2004.03.122.

55. N. Liu and C. Y. Yam, "First-Principles Study of Intrinsic Defects in Formamidinium Lead Triiodide Perovskite Solar Cell Absorbers," *Physical Chemistry Chemical Physics* 20 (2018): 6800–6804, https://doi.org/10.1039/C8CP00280K.

56. M. Hudlicky, "Chemical Shifts of Fluorine in Hydrogen Fluoride and Fluoride Ion," *Journal of Fluorine Chemistry* 28 (1985): 461–472, https://doi.org/10.1016/S0022-1139(00)81136-7.

57. T. Lu, "A Comprehensive Electron Wavefunction Analysis Toolbox for Chemists, Multiwfn," *Journal of Chemical Physics* 161 (2024): 082503, https://doi.org/10.1063/5.0216272.

58. T. Lu and F. Chen, "Multiwfn: A Multifunctional Wavefunction Analyzer," *Journal of Computational Chemistry* 33 (2012): 580–592, https://doi.org/10.1002/jcc.22885.

59. T. Lu and F. Chen, "Atomic Dipole Moment Corrected Hirshfeld Population Method," *Journal of Theoretical and Computational Chemistry* 11 (2012): 163–183, https://doi.org/10.1142/S0219633612500113.

60. S. Qin, C. Lu, Z. Jia, et al., "Constructing Monolithic Perovskite/Organic Tandem Solar Cell with Efficiency of 22.0% via Reduced Open-Circuit Voltage Loss and Broadened Absorption Spectra," *Advanced Materials* 34 (2022): 2108829, https://doi.org/10.1002/adma.202108829.

61. Y. Ding, B. Ding, P. Shi, et al., "Cation Reactivity Inhibits Perovskite Degradation in Efficient and Stable Solar Modules," *Science* 386 (2024): 531–538, https://doi.org/10.1126/science.ado6619.

62. E. A. Duijnstee, B. M. Gallant, P. Holzhey, et al., "Understanding the Degradation of Methylenediammonium and Its Role in Phase-Stabilizing Formamidinium Lead Triiodide," *Journal of the American Chemical Society* 145 (2023): 10275–10284, https://doi.org/10.1021/jacs.3c01531.

63. W. T. M. Van Gompel, R. Herckens, G. Reekmans, et al., "Degradation of the Formamidinium Cation and the Quantification of the Formamidinium–Methylammonium Ratio in Lead Iodide Hybrid Perovskites by Nuclear Magnetic Resonance Spectroscopy," *Journal of Physical Chemistry C* 122 (2018): 4117–4124.

64. J. Wang, H. Tao, S. Li, R. Wang, J. Qian, and X. Zhang, "In Situ Generation of Hydrogen Fluoride for F-Doping of Perovskite Quantum Dots," *Chemistry of Materials* 38 (2026): 3611–3618, https://doi.org/10.1021/acs.chemmater.6c00080.

65. X. Zhao, P. Zhang, T. Liu, et al., "Operationally Stable Perovskite Solar Modules Enabled by Vapor-Phase Fluoride Treatment," *Science* 385 (2024): 433–438, https://doi.org/10.1126/science.adn9453.

66. M. V. Khenkin, E. A. Katz, A. Abate, et al., "Consensus Statement for Stability Assessment and Reporting for Perovskite Photovoltaics Based on ISOS Procedures," *Nature Energy* 5 (2020): 35–49, https://doi.org/10.1038/s41560-019-0529-5.

Supporting Information

Additional supporting information can be found online in the Supporting Information section.

Supporting File: aenm71396-sup-0001-SuppMat.docx.